

# Complex SAR Image Compression Based on Directional Lifting Wavelet Transform With High Clustering Capability

Xingsong Hou, Jing Yang, Guifeng Jiang, and Xueming Qian, *Member, IEEE*

**Abstract**—We propose two synthetic aperture radar (SAR) complex image compression schemes based on DLWT\_IQ and DLWT\_FFT. DLWT\_IQ encodes the real parts and imaginary parts of the images using directional lifting wavelet transform (DLWT) and bit plane encoder (BPE), while DLWT\_FFT encodes the real images converted by fast Fourier transform (FFT). Compared with discrete wavelet transform-IQ (DWT\_IQ), DLWT\_IQ improves the peak signal-to-noise ratio (PSNR) up to 1.28 dB and reduces the mean phase error (MPE) up to 21.74%; and compared with DWT\_FFT, DLWT\_FFT improves the PSNR up to 1.22 dB and reduces the MPE up to 20.32%. Moreover, the proposed schemes increase the PSNR up to 3.34 dB and decrease the MPE up to 50.43% as compared with the set partitioning in hierarchical trees (SPIHT) algorithm. In addition to this, we observe a novel phenomenon, that is, DLWT with direction prediction achieves a higher clustering capability for complex SAR images than DWT. Then, coding algorithm based on DLWT requires fewer coding bits than DWT for the same number of coding coefficients, and DLWT outperforms DWT in terms of rate-distortion performance even if the K-term nonlinear approximation of DWT is better than that of DLWT.

**Index Terms**—Complex synthetic aperture radar (SAR) image, directional lifting wavelet transform (DLWT), image coding.

## I. INTRODUCTION

**S**YNTHETIC aperture radar (SAR), which is an all-time, all-weather microwave imaging system, is an important tool for achieving information in the application field of microwave remote sensing. With synthetic aperture radar (SAR) developing along the directions of high resolution, multipolarization, multiband, and multimode, the quantity of SAR image data rises steadily. Data compression technology is an effective way to alleviate the pressure of transmission and storage on SAR system. The complex SAR image, which consists of amplitude and phase, is the first-level image data of the SAR system. The phase information fidelity in complex SAR image is crucial to some special applications, such as interferometry and moving target detection. Therefore, complex SAR image

Manuscript received August 28, 2010; revised January 29, 2011, June 17, 2011, and December 10, 2011; accepted February 12, 2012. Date of publication July 23, 2012; date of current version December 19, 2012. This work was supported by National Natural Science Foundation of China (project 60602024, 60903121, and 61173109), and 2009 Campus Research Foundation of Xi'an Jiaotong University (project xjj2009042) and "the Fundamental Research Funds for the Central University" (project xjj2012023).

The authors are with the School of Electronics and Information Engineering, Xi'an Jiaotong University, Xi'an 710049, China (e-mail: houxs@mail.xjtu.edu.cn; qianxm@mail.xjtu.edu.cn).

Color versions of one or more of the figures in this paper are available online at <http://ieeexplore.ieee.org>.

Digital Object Identifier 10.1109/TGRS.2012.2203309

compression requires not only reasonable amplitude fidelity but also high phase information accuracy, which is different from the ordinary optical image compression. Furthermore, compared with optical images, complex SAR images exhibit significantly higher dynamic range and less spatial correlation. Thus, common optical image compression algorithms are not suitable for the compression of complex SAR images.

Efficient representation is important to the compression of complex SAR images. Typically, 2-D-Fourier transform (2-D-FT) is used as the representation of complex SAR images. However, the energy of the coefficients of 2-D FT on the complex SAR image distributes in the whole frequency domain. Generally, the frequency signals are divided into real and imaginary parts, and quantized with Lloyd-Max quantizer [1], [2]. However, the compression ratios of the frequency-domain compression algorithms are almost limited in 10.4:1 [1] or 9.8:1 [2], which are not very high. Wavelet transform can locally analyze time and frequency in multiscale [3] and shows very strong decorrelation ability [4]. As it is particularly suitable for non-stationary signal processing, wavelet transform has been applied to complex SAR image compression [5]–[8].

Currently, most compression algorithms of complex SAR image adopt the traditional wavelet transform. However, for the complex SAR images, which are rich in edges and texture, traditional wavelet transform does not show efficient representation. Dong *et al.* [9] proposed an algorithm which extracted edges of SAR image with wedgelet transform and encoded the edges and texture separately. Li *et al.* [10] used 2-D oriented wavelet transform for remote sensing compression. The SAR images used in [9], [10] are not complex SAR images. To the best of our knowledge, directional wavelet transform has not been applied to the compression of complex SAR images. Directional wavelet transform achieves the direction extraction while keeping the property of multiscale analysis of discrete wavelet transform (DWT). Directional wavelet transform can be divided into two classes: frequency-domain transform and spatial-domain transform. The frequency-domain directional wavelet transform, such as contourlet [11], which continuously performs directional filter on the high-frequency subbands of wavelet transform, gives an efficient representation of the edges at the cost of high redundancy. The spatial-domain directional wavelet, such as directional lifting wavelet transform (DLWT), employs direction prediction for wavelet decomposition, which adapts the wavelet transform direction to the image edges. DLWT [12]–[14] integrates spatial direction prediction into the wavelet transform lifting framework, provides an efficient

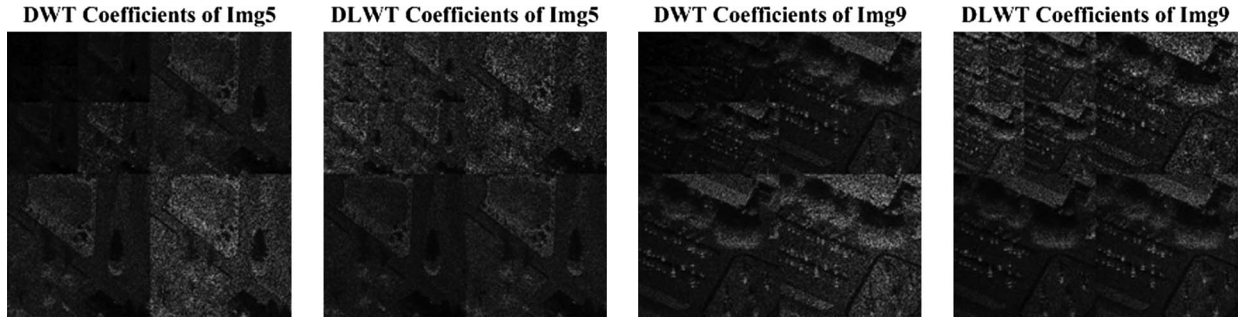


Fig. 1. Comparison of three level decomposition coefficients of DWT and DLWT.

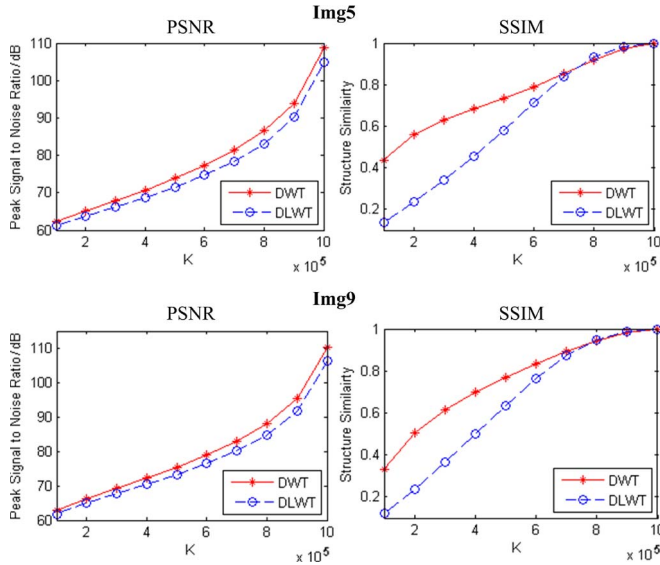


Fig. 2. Best  $K$ -term nonlinear approximation of DWT and DLWT in PSNR and SSIM.

representation of edges along multiple directions of images, and thus reduces the energy of high-frequency bands and achieves more energy clustering. Testing results of the complex SAR image in Fig. 1 shows that energy of alternating current (ac) coefficients of DLWT is much smaller than that of DWT and thus increases the efficiency of the subsequent coding. For *Img5*, the energy percentage of ac coefficients is 94.26% for DLWT while it is 99.90% for DWT. For *Img9*, energy percentage of ac coefficients is 96.99% for DLWT while it is 99.90% for DWT.

In this paper, we propose an efficient representation of SAR images using DLWT. As the real parts and imaginary parts of complex SAR image as well as the real image of fast FT (FFT) are rich in edges, two complex SAR image coding schemes using DLWT are proposed. The first scheme directly encodes real parts and imaginary parts of complex SAR images using the CCSDS algorithm [15], [16], which replaces DWT by DLWT. The second scheme first converts a complex image into a real image using FFT, and then encodes the real image in the CCSDS coding algorithm which also replaces DWT by DLWT. Compared with the original CCSDS image coding schemes using DWT, the proposed two coding schemes show significant performance gain not only in amplitude peak signal-to-noise ratio (PSNR) but also in mean phase error (MPE).

It is interesting that, as shown in Fig. 2, the best  $K$ -term nonlinear approximation [3] of DWT outperforms that of DLWT

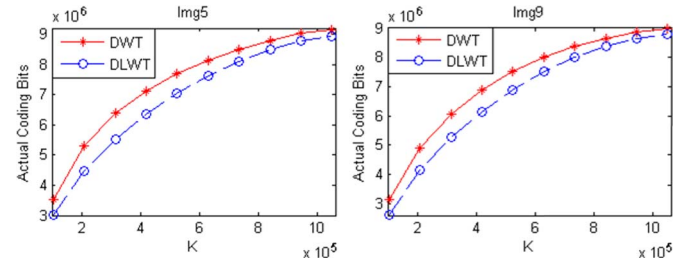


Fig. 3. Bits consuming of DLWT and DWT.

in terms of PSNR and structure similarity (SSIM) [17], [18]. However, the coding algorithm based on DLWT achieves better rate-distortion performance than that of DWT. It is because the rate-distortion performance of coding algorithm is determined not only by the number of significant coefficients, but also by the position distribution of significant coefficients, i.e., the clustering capability of significant coefficients.

The coding bits of significant coefficients with CCSDS algorithm are shown in Fig. 3. Compared with the results in Fig. 2, we can see that although DLWT with  $K$ -term nonlinear approximation gets less PSNR and SSIM than DWT, DLWT coefficients need less actual coding bits for the same number of significant coefficients than DWT. Therefore, at the same bit rate, we can encode more coefficients with DLWT than DWT, then DLWT may outperform DWT in terms of rate-distortion performance eventually. DLWT consuming less coding bits is due to the better clustering capability, which will be explained in Part C of Section II.

The remainder of this paper is given as follows. Section II describes the representation using DLWT and CCSDS coding algorithm. Two DLWT-based complex SAR image coding algorithms are proposed in Section III. Section IV gives extensive experimental results and discussions on the results. Section V summarizes this paper.

## II. DLWT-BASED COMPLEX SAR IMAGE REPRESENTATION WITH HIGH CLUSTERING CAPACITY

Efficient representation is crucial to compression since it determines the compression efficiency. This paper employs DLWT as the representation of complex SAR image compression, which exhibits higher clustering capability for complex SAR images than DWT and thus more suitable for source coding.

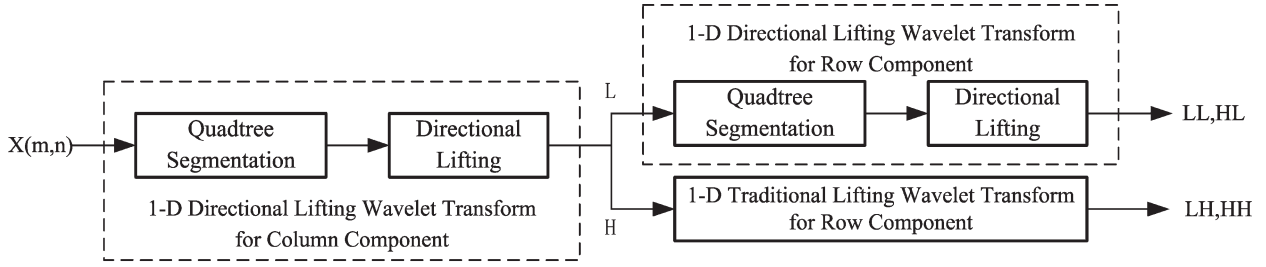


Fig. 4. Two-Dimensional DLWT.

### A. Two-Dimensional DLWT

Two-dimensional DLWT involves two separable transforms, i.e., vertical transform and horizontal transform. Fig. 4 is the schematic of 2-D DLWT. Let  $X(m,n)$  be a 2-D input signal, where  $m$  and  $n$  indicate row index and column index, respectively. First, perform 1-D DLWT on each image column, generating a vertical low-pass subband (L) and a vertical high-pass subband (H). Second, perform 1-D DLWT on each row of L and just perform 1-D DWT on each row of H, as the energy of H is not very high. After one-level decomposition, one low-pass subband (LL) and three high-pass subbands (LH, HL, and HH) are produced. In other words, the subband decomposition structure of 2-D DLWT is identical with 2-D DWT. Decomposition process of DLWT can be extended to any desired level.

As DLWT does not transform along the fixed direction like DWT, the selected filtering directions need to be encoded as side information. In order to reduce the overhead bits for the direction information, the image is divided into regions of approximately uniform edge orientations. In the local region, all the pixels are predicted and updated along the uniform direction which is selected in a rate-distortion optimal sense. In the vertical transform and horizontal transform,  $X(m,n)$  and low-pass subband (L) are adaptively divided into variable-size regions with a quadtree segmentation method.

1) *Quadtree Segmentation*: The quadtree segmentation method [19], a bottom-up algorithm in the unconventional sense, is chosen to construct an optimal quadtree which balances the distortion from prediction with the rate of coding the segmentation tree (including tree structure and direction of each leaf node). The distortion for representing block  $X_k$  with a single leaf is

$$D(X_k) = \sum_m \sum_n \left| x_o(m,n) - \frac{1}{2} (x_e^d(m,n) + x_e^d(m+1,n)) \right| \quad (1)$$

where  $m$  and  $n$  indicate the indexes of row and column, respectively,  $x_o(m,n)$  denotes odd pixel in the block,  $x_e^d(m,n)$  and  $x_e^d(m+1,n)$  are even pixels in the direction  $d$ . As the quadtree structure is encoded with one bit per node, the rate for representing block  $X_k$  with a single leaf is

$$R(X_k) = 1 + R(d - dp) \quad (2)$$

where  $R(d - dp)$  denotes the number of bits to encode the prediction residual,  $dp$  is the direction predictor. The direction predictor is the dominant direction selected from the direction of adjacent blocks. The prediction residual of direction is encoded with Exp-Golomb in H.264 [20].

2) *Directional Lifting*: Similar to the conventional lifting, a directional lifting stage also comprises four steps, i.e., split, predict, update and normalize, and the prediction and update steps are implemented along the optimal direction. In this paper, the improved weighted lifting scheme of WAL [13] is adopted to implement the directional lifting. In the prediction step, the odd pixels located at integer position are predicted from the neighboring even pixels along the optimal direction of the local region. The prediction step of vertical transform can be expressed as

$$h(m,n) = x_o(m,n) - \sum_{i=0}^1 p_i x_e^d(m+i,n) \quad (3)$$

where  $p_i$  is the high-pass filter coefficient,  $x_e^d(m+i,n)$  denotes the neighboring even subset along the optimal direction  $d$ . The  $d$  is one of the nine directions (i.e.,  $0, \pm 1/4, \pm 1/2, \pm 3/4$  and  $\pm 1$ ), which means that  $x_e^d(m+i,n)$  may be integer pixel or subpixel. The subpixel with quarter pixel accuracy is interpolated by the neighboring even integer pixels, and the interpolation method used here is directional interpolation presented in [13]. In the update step, the obtained high-frequency coefficients are likewise distributed to those even pixels that are used to calculate them in the prediction step. The update step of vertical transform can be expressed as

$$l(m,n) = x_e(m,n) + \sum_{j=-1}^0 u_j [\beta_j x_o^d(m+j,n) + \gamma_j] \quad (4)$$

where  $u_j$  is the low-pass filter coefficients,  $\beta_j$  and  $\gamma_j$  are amendment parameters,  $x_o^d(m+j,n)$  is the weighted function of high-pass coefficients

$$x_o^d(m+j,n) = \sum_k w_{j,k} x_o(m,n) \quad (5)$$

where  $w_{j,k}$  is the weighted parameter. In the above lifting stage, the parameters of  $\beta_j$ ,  $\gamma_j$ , and  $w_{j,k}$  are chosen according to the literature [13];  $p_i$  and  $u_j$  are determined by the wavelet filter.

### B. CCSDS Coding Algorithm

The CCSDS image compression standard is proposed in 2005 by the consultative committee for space data systems. It is simple and of low computational complexity, and is commonly applied to remote sensing [15].

The CCSDS image compression algorithm [16] consists of two functional parts, i.e., three-level DWT and bit plane encoder (BPE). DWT is similar with DLWT, but without the

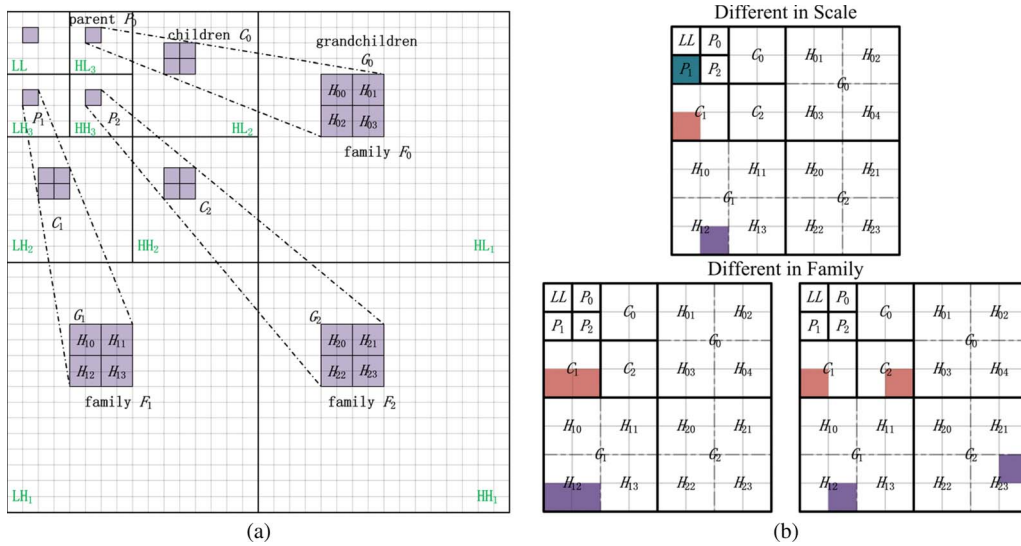


Fig. 5. Block of wavelet coefficients, (a) schematic of wavelet-transformed image and (b) schematic of one  $8 \times 8$  blocks.

TABLE I  
EXAMPLE OF CODING SYMBOLS GENERATED BY BPE

Coefficient Position		Coding Symbols							Symbol Length	Scale	Family
		TypeP	TranB	TranD	TypeC	TranG	TranH	TypeH			
Different in Scale	$P_1$	010	0	/	/	/	/	/	4	3	/
	$C_1$	000	1	010	0010	000	/	/	14	2	/
	$G_1 \rightarrow H_{12}$	000	1	010	0000	010	0010	0001	22	1	/
Different in Family	Only $C_1$	000	1	010	0011	000	/	/	14	2	1
	$C_1$ and $C_2$	000	1	011	0010,0001	000	/	/	18	2	2
	Only $H_{12}$	000	1	010	0000	010	0010	0011	22	1	1
	$H_{12}$ and $H_{23}$	000	1	011	0000,0000	011	0010,0001	0001,0100	34	1	2

direction lifting parts and quadtree segmentation. BPE can be seen as a zero-tree coding algorithm, which organizes the wavelet coefficients corresponding to the same area of the original image as  $8 \times 8$  block (Fig. 5). Each block includes a direct current (dc) coefficient and 63 ac coefficients which are from three families on the horizontal, vertical, and diagonal directions. According to the scale factor of the subband in which the coefficients locate, the coefficients of each family are divided into parents ( $P$ ), children ( $C$ ), and grandchildren ( $G$ ). When encoding each block, the correlations among subbands are used, that is, the significance of the descendants can be judged from their ancestors in each family. To limit the effect of transmission errors such as packet loss to a small area, the blocks are organized as segments which are separately encoded and outputted with a segment header.

When encoding each segment, the segment header is first output, and then the dc coefficients and ac coefficients are encoded from top to bottom of the bit planes. DC coefficients of the segment are all or partially encoded before ac coefficients according to the dynamic range of dc coefficients. If the dynamic range is very small, the dc coefficients are all encoded; otherwise, the dc coefficients are first quantized with the quantization step determined by the comparison between

the dynamic ranges of dc coefficients and ac coefficients, and then the quantized dc coefficients are encoded. In each bit plane, the ac coefficients are encoded in the parent-children-grandchildren order. The significant bits are encoded first, and then the refinement bits are output directly. If the significant bit is 0, the current block does not need to be encoded.

### C. Clustering Capability of DLWT

In Section I, we mentioned that DLWT shows worse  $K$ -term nonlinear approximation, but performs better in coding performance. These results lead to a contradiction of  $K$ -term nonlinear approximation and coding performance. To explain this phenomenon, clustering capability of DLWT and DWT is compared in this part. We find that DLWT shows a higher clustering capability and the coding algorithm can benefit from the higher clustering capability when compared with DWT.

1) *Influence on Coding Algorithm of the Position of Significant Coefficients:* In the BPE, if the positions of significant coefficients are different, the lengths of the needed coding symbols are also different. Table I shows an example of the coding symbols generated by BPE. The list of descendants in family  $i$ , denoted  $D_i$ , is defined as  $D_i = \{C_i, G_i\}$ . The

TABLE II  
ENERGY DISTRIBUTION OF DWT AND DLWT IN EACH SCALE

Image Type	Representation	Scale			
		<i>LL</i>	<i>P</i>	<i>C</i>	<i>G</i>
<i>I</i>	<i>DWT</i>	0.0141	0.0135	0.1010	0.8714
	<i>DLWT</i>	0.0348	0.0667	0.2256	0.6729
<i>Q</i>	<i>DWT</i>	0.0158	0.0133	0.0990	0.8719
	<i>DLWT</i>	0.0369	0.0671	0.2258	0.6702
<i>FFT</i>	<i>DWT</i>	0.9710	0.0083	0.0036	0.0171
	<i>DLWT</i>	0.9711	0.0090	0.0046	0.0154

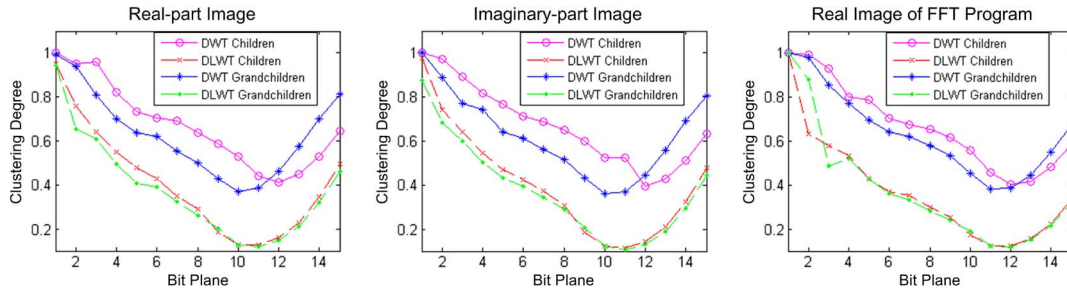


Fig. 6. Family clustering capability of DWT and DLWT.

list of descendants in a block, denoted  $B$ , is defined as  $B = \{D_0, D_1, D_2\}$ . First, parents coefficients are coded by  $TypeP$ .  $TypeP_i = 1$  means  $P_i$  is in the current bit plane  $b$ . Then, if any coefficient in set  $B$  is in the current coding bit plane,  $TranB$  is set to 1, otherwise,  $TranB$  is set to 0. When  $TranB$  is 1,  $D_i$  is checked. If any coefficients of  $D_i$  are in the current coding bit plane,  $TranD_i$  is set to 1. If  $TranD_i \neq 0$ ,  $C_i$  is coded. Coding of children coefficients is finished now.  $TranG$  and  $TranH$  are used to position the grandchildren coefficients. If  $TranG_i = 1$ ,  $TranH_{ij}$  is further coded, only when  $TranH_{ij} = 1$ , coefficients in  $H_{ij}$  are going to be coded. Coefficient positions of Table I are shown in Fig. 5(b). When coefficient distributes in different positions, coding symbol lengths are different. Clearly, coefficients distributions, including scale distribution and family distribution, influence the coding symbols. Therefore, clustering capability of DLWT is analyzed following these two aspects.

2) *Clustering Capability of DLWT in Scale*: Due to the directional lifting of DLWT, energy distribution of DLWT is much different from DWT. Decomposition using DLWT can significantly reduce the energy of high-pass coefficients and cluster the energy of coefficients to the low-pass subbands or the big scale high-pass subband, i.e.,  $P$  and  $C$ . This regularity of distribution is contributed to image coding. Nineteen images, sized  $1024 \times 2048$ , are tested in this experiment, which are obtained from the website of Sandia National Laboratory of America [21]. In this test, CDF 9/7 is used for DLWT and DWT, and three-level wavelet decomposition is made.

In Table II, three types of images are tested.  $I$  and  $Q$  separately present the real and imaginary parts of complex SAR images, and FFT presents the real image converted by the FFT scheme, shown in Fig. 8. Data in Table II shows energy proportions in every scales, which are the mean value

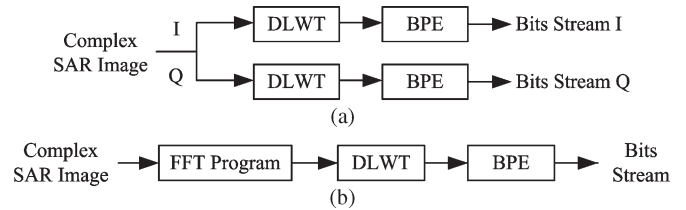


Fig. 7. Compression of complex SAR image using DLWT in (a) DLWT\_IQ Scheme and (b) DLWT\_FFT Scheme.

corresponding to the 19 images. Clearly, for the real-part and imaginary-part images, energy proportions of DLWT in  $LL$  and the big scale high-pass subband, i.e.,  $P$  and  $C$ , are much bigger than DWT. For the real images of FFT program, energy proportions of DLWT in  $LL$  are almost the same than DWT, but energy proportions of the big scale high-pass subband are a little bit bigger than that of DWT. As Table I shows, scale distribution of significant coefficients can affect the coding bits a lot, therefore DLWT showed better scale clustering capability can save the coding bits.

3) *Clustering Capability of DLWT in Family*: As Table I shows, if the significant coefficients can be clustered in fewer families, the number of needed coding bit is much fewer. DLWT can also show such advantage of clustering. Fig. 6 shows the contrast of DWT and DLWT in family clustering. Data in Fig. 6 presents the mean clustering degree for the 19 images, calculated by the following equation:

$$\text{ClusteringDegree}(b) = \frac{\text{FamilyNumber}(b)}{\text{CoefficientNumber}(b)} \quad (6)$$

where  $b$  refers to the current bit plane.  $\text{FamilyNumber}(b)$  indicates the number of non-empty families in bitplane  $b$ , and  $\text{CoefficientNumber}(b)$  means the number of coefficients in

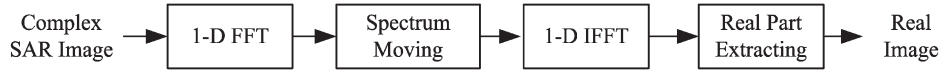


Fig. 8. FFT program.

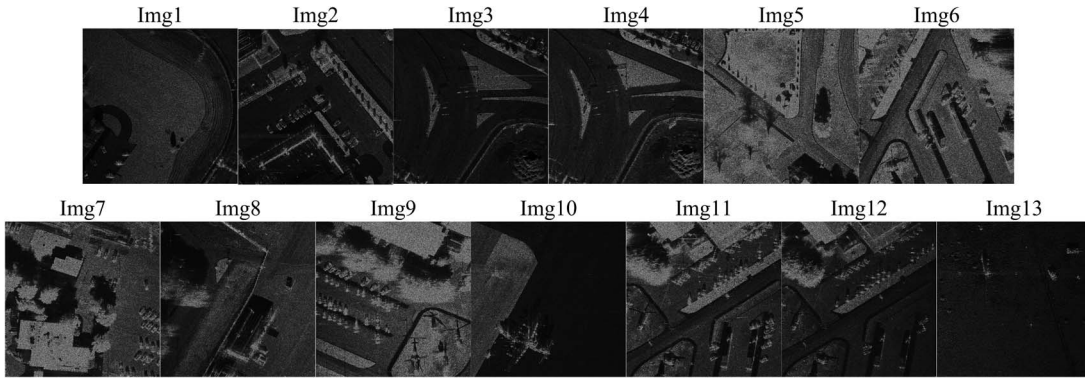


Fig. 9. Real-parts of thirteen testing images.

bitplane  $b$ . No matter for the children coefficients or for the grandchildren coefficients, DLWT shows significant better family clustering than DWT. In FFT algorithm, although DLWT does not show much improving in scale clustering capability, it performs much better in family clustering capabilities, which also can save a lot of coding bits in CCSDS-based algorithms.

In a word, clustering capability can greatly affect the coding performance, meanwhile DLWT shows better clustering capability, not only in scale clustering capability, but also in family clustering capability. Therefore, DLWT may perform better than DWT in coding algorithms although its K-term approximation capability is not as good as that of DWT.

### III. PROPOSED IMAGE CODING ALGORITHMS

Complex SAR image can generally be compressed in two kinds of images: real and imaginary part of original complex SAR image, and real image with FFT converted from original complex SAR image. Brandfass *et al.* [6] presented that complex SAR image can be first converted into a real image of the same amount and without loss of any phase information, then performed wavelet representation and zero-tree encoding on the real image. The real image achieved through FFT scheme is equivalent to the interpolation image of the real-part image of complex SAR image. Both the real image and the real part/imaginary part of the complex SAR image are rich in edges.

DLWT implements the prediction and update steps along the optimal direction and can give a representation of the edges along multiple directions in images when compared with DWT. As mentioned in Section II, DLWT can effectively improve the clustering capability compared to DWT. Therefore, two complex SAR image coding schemes using DLWT are proposed as follows:

- **DLWT\_IQ**: Divide the complex image into two images, i.e., real part and imaginary part, then performs DLWT on each image, and finally encodes the wavelet coefficients with a zero-tree coding algorithm. Two separate

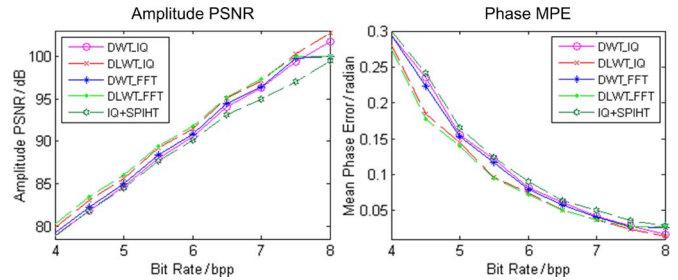


Fig. 10. Comparison of coding performance in amplitude PSNR and MPE.

bits streams with the same bit rates are obtained in this algorithm.

- **DLWT\_FFT**: Convert the complex image into a real image by adopting FFT scheme, then performs DLWT on the real image, and finally encodes the wavelet coefficients with a zero-tree coding algorithm.

In both of these two schemes, DLWT is implemented with three-level CDF 9/7 wavelet decomposition, and the zero-tree coding algorithm is the BPE of the CCSDS image compression standard. The algorithm structures of the two schemes are presented in Fig. 7.

Fig. 8 shows the implementation diagram of FFT program. The realization process of FFT program is: first, apply 1-D FFT transform on the complex SAR image and shift the negative frequency band to the positive side, which makes the original signal bandwidth doubled and the original frequency signal concentrated in the positive side; second, perform 1-D IFFT transform and obtain a complex signal with data volume doubled; finally, represent the complex signal with its real part because the real part and imaginary part of the complex signal satisfy the Hilbert transform. The spectrum movement is equivalent to supplement zeros on the negative side of the frequency signal and makes the bandwidth doubled; therefore, the complex signal which is the output signal of the inverse FFT transform is equivalent to interpolate the complex SAR image by every two pixels on the dimension of transform.

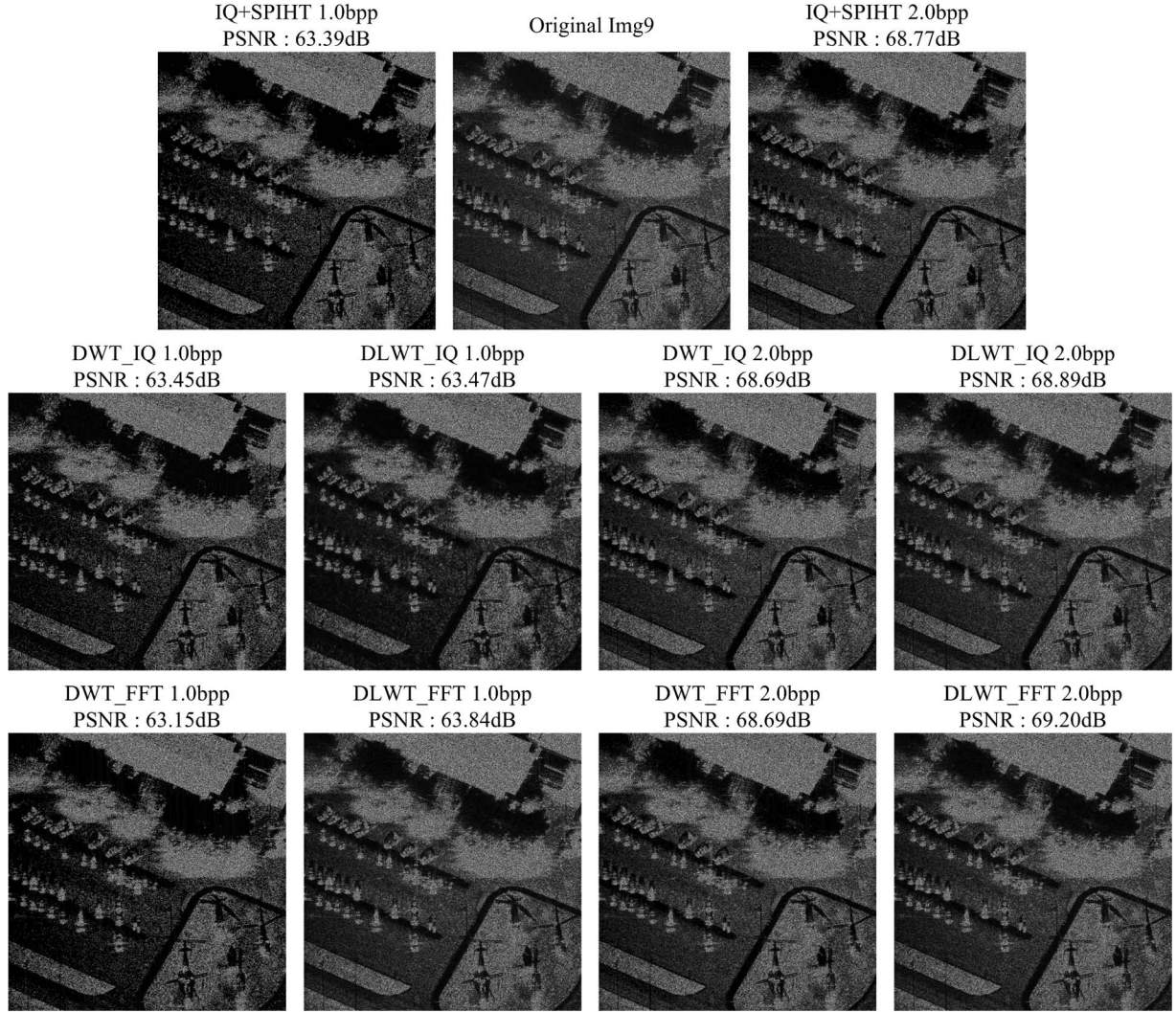


Fig. 11. Visual comparison of *Img9* at 1.0 bpp and 2.0 bpp.

#### IV. EXPERIMENTAL RESULTS AND ANALYSIS

We perform experiments on 13 complex SAR images of sizes  $1024 \times 1024$ , where each pixel of either real or imaginary parts is represented using 16-bit signed integer [21]. In order to facilitate data processing, each pixel of either real or imaginary parts of the original images is of 17-bit signed integer, and the test images are obtained by removing the lowest bit of the original images. Fig. 9 shows the real part of the 13 tested images, and the imaginary part looks almost the same and thus omitted here.

We use PSNR and MPE to measure the amplitude and phase distortions of the complex SAR images, respectively, given by

$$\text{PSNR} = 10 \times \log_{10} \left( \frac{65535^2}{\text{MSE}} \right) \quad (7)$$

$$\text{MPE} = \frac{1}{MN} \sum_{i=1}^M \sum_{j=1}^N |\varphi_{ij} - \tilde{\varphi}_{ij}| \quad (8)$$

where MSE refers to the mean square error,  $M$  and  $N$  denote the number of pixels along column and row, respectively, and

$\varphi_{ij}$  and  $\tilde{\varphi}_{ij}$  represent the phases at row  $i$  and column  $j$  of the original and the decoded images, respectively.

##### A. Coding Performance of the Proposed Coding Algorithm

We show in Fig. 10 the coding performances of DLWT\_IQ, DLWT\_FFT, DWT\_IQ, DWT\_FFT, and IQ+SPIHT for *Img9*. The set partitioning in hierarchical tree (SPIHT) employs CDF9/7 wavelet and decomposes for seven levels [22], using the Matlab and C++ implementations available online at [23]. The only difference between DWT\_IQ and DLWT\_IQ, as well as DWT\_FFT and DLWT\_FFT, is that the former employs DWT as the representation while the latter employs DLWT. As shown in Fig. 10, DLWT\_IQ outperforms DWT\_IQ by achieving PSNR improvements up to 1.28 dB and MPE reduction up to 0.144, and DLWT\_FFT outperforms DWT\_FFT by achieving PSNR improvements to 1.22 dB and MPE reduction up to 0.129. At the moderate bit rates, compared with DWT\_IQ and DLWT\_IQ, DWT\_FFT and DLWT\_FFT show performance improvements via increasing PSNR up to 0.44 dB and reducing MPE up to 0.0241. Compared with the SPIHT, DLWT\_IQ

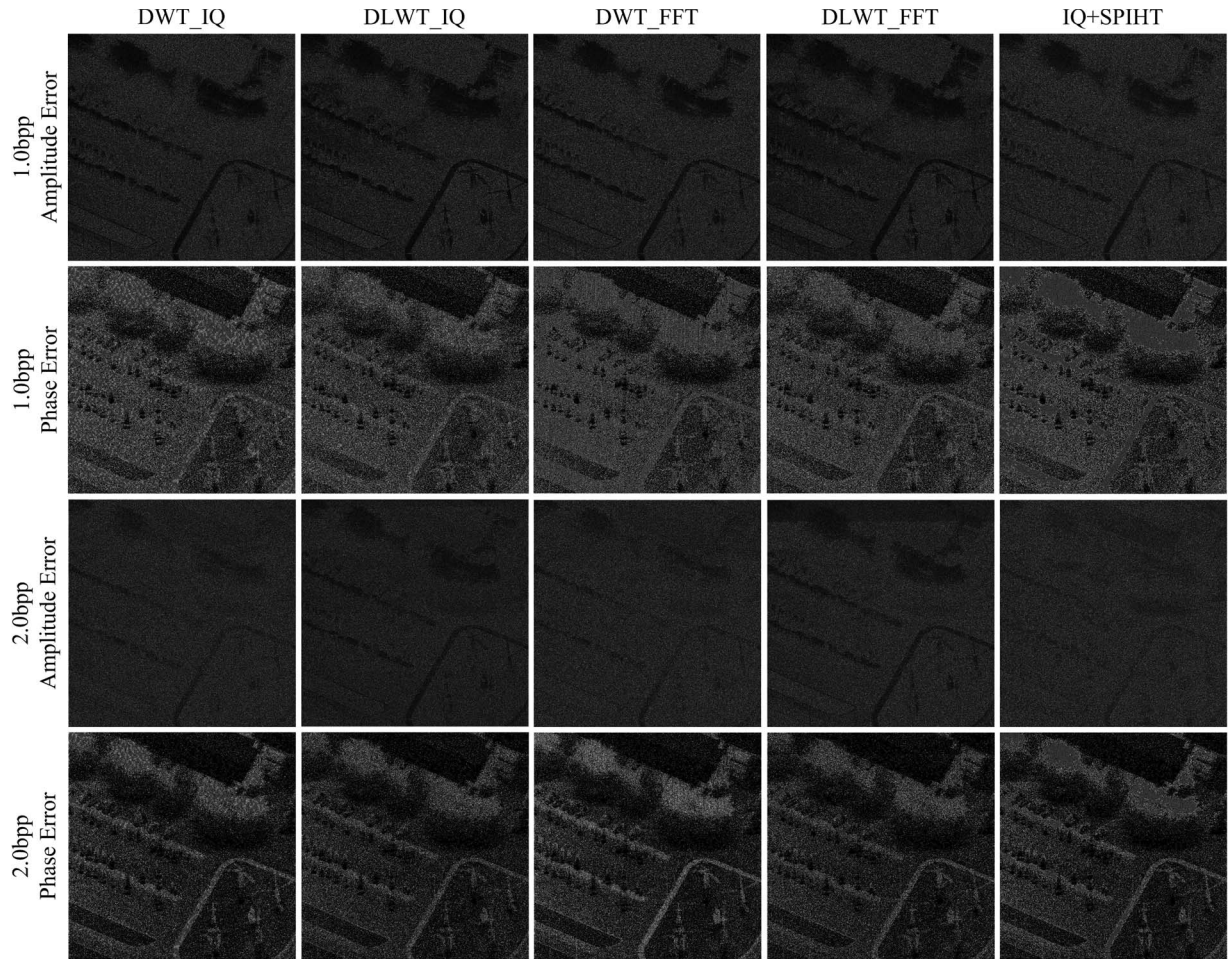


Fig. 12. Error maps of amplitude and phase of *Img9*.

TABLE III  
COMPARISONS OF CODING PERFORMANCE IN PSNR (dB)

Image	1.0 bpp					3.0 bpp					5.0 bpp				
	<i>DWT</i> <i>_IQ</i>	<i>DLWT</i> <i>_IQ</i>	<i>DWT</i> <i>_FFT</i>	<i>DLWT</i> <i>_FFT</i>	<i>IQ+</i> <i>SPIHT</i>	<i>DWT</i> <i>_IQ</i>	<i>DLWT</i> <i>_IQ</i>	<i>DWT</i> <i>_FFT</i>	<i>DLWT</i> <i>_FFT</i>	<i>IQ+</i> <i>SPIHT</i>	<i>DWT</i> <i>_IQ</i>	<i>DLWT</i> <i>_IQ</i>	<i>DWT</i> <i>_FFT</i>	<i>DLWT</i> <i>_FFT</i>	<i>IQ+</i> <i>SPIHT</i>
<i>Img1</i>	70.13	70.88	70.15	71.20	70.83	81.02	81.66	81.14	81.84	81.11	92.36	93.73	92.44	93.97	91.73
<i>Img4</i>	73.88	74.51	73.74	74.97	74.28	83.52	84.30	83.51	84.53	83.33	95.20	95.82	95.21	95.87	93.91
<i>Img6</i>	63.29	63.33	63.04	63.72	63.33	73.23	74.07	73.38	74.31	73.24	84.39	85.29	84.60	85.57	84.24
<i>Img7</i>	64.10	64.67	64.07	65.02	64.50	75.05	75.81	75.30	76.04	75.30	86.48	87.72	86.91	88.03	86.20
<i>Img10</i>	75.05	75.02	74.31	75.36	75.04	84.66	85.33	84.60	85.55	84.57	95.65	96.46	95.69	96.42	94.50
<i>Img11</i>	66.01	67.39	66.14	67.80	66.76	76.95	77.80	77.05	78.18	77.00	88.65	89.61	88.91	89.82	88.18
<i>Img13</i>	75.25	75.36	75.14	75.84	75.52	84.71	85.41	84.66	85.68	84.56	95.83	96.60	95.86	96.62	94.64

shows up to 3.34 dB gain in PSNR and 0.09 reduction in MPE, and DLWT\_FFT shows up to 2.97 dB gain in PSNR and 0.1 reduction in MPE.

Fig. 11 compares the reconstructed amplitude images at the rates of 1.0 and 2.0 bit per pixel (bpp) for DWT\_IQ, DLWT\_IQ, DWT\_FFT, DLWT\_FFT, and SPIHT, to show the visual quality of the five compression schemes. It is seen that DLWT\_FFT achieves the best visual quality. Fig. 12 shows the error maps

of amplitudes and phases of the images used in Fig. 11. Ideally, the error maps should be uniform over all pixels. However, for all schemes, it is not the case, which shows the necessity of improving the existing coding schemes.

Finally, in Tables III and IV, we show the coding performances of the five compression schemes at the rates 1.0, 3.0 and 5.0 bpp. Seven complex SAR images are used. The DLWT-based coding schemes outperform the DWT-based counterparts

TABLE IV  
COMPARISONS OF CODING PERFORMANCE IN MPE (RADIAN)

Image	1.0 bpp					3.0 bpp					5.0 bpp				
	<i>DWT</i>	<i>DLWT</i>	<i>DWT</i>	<i>DLWT</i>	<i>IQ+</i>	<i>DWT</i>	<i>DLWT</i>	<i>DWT</i>	<i>DLWT</i>	<i>IQ+</i>	<i>DWT</i>	<i>DLWT</i>	<i>DWT</i>	<i>DLWT</i>	<i>IQ+</i>
	<i>_IQ</i>	<i>_IQ</i>	<i>_FFT</i>	<i>_FFT</i>	<i>SPIHT</i>	<i>_IQ</i>	<i>_IQ</i>	<i>_FFT</i>	<i>_FFT</i>	<i>SPIHT</i>	<i>_IQ</i>	<i>_IQ</i>	<i>_FFT</i>	<i>_FFT</i>	<i>SPIHT</i>
<i>Img1</i>	1.401	1.253	1.465	1.273	1.242	0.539	0.468	0.537	0.469	0.522	0.152	0.139	0.150	0.132	0.161
<i>Img4</i>	1.323	1.303	1.339	1.313	1.290	0.462	0.422	0.477	0.413	0.469	0.132	0.122	0.136	0.122	0.143
<i>Img6</i>	1.383	1.306	1.334	1.362	1.329	0.494	0.485	0.492	0.480	0.498	0.145	0.135	0.144	0.133	0.152
<i>Img7</i>	1.500	1.333	1.703	1.421	1.353	0.623	0.516	0.613	0.517	0.601	0.173	0.160	0.168	0.156	0.138
<i>Img10</i>	1.345	1.366	1.499	1.444	1.359	0.461	0.462	0.461	0.451	0.461	0.140	0.129	0.145	0.132	0.153
<i>Img11</i>	1.489	1.335	1.351	1.356	1.312	0.523	0.458	0.532	0.443	0.533	0.156	0.133	0.153	0.131	0.164
<i>Img13</i>	1.387	1.245	1.420	1.330	1.336	0.462	0.451	0.167	0.441	0.464	0.138	0.125	0.140	0.125	0.152

TABLE V  
ALMOST LOSSLESS CODING BITRATES (bpp)

Coding Algorithm	Image												
	<i>Img1</i>	<i>Img2</i>	<i>Img3</i>	<i>Img4</i>	<i>Img5</i>	<i>Img6</i>	<i>Img7</i>	<i>Img8</i>	<i>Img9</i>	<i>Img10</i>	<i>Img11</i>	<i>Img12</i>	<i>Img13</i>
<i>DWT_IQ</i>	7.304	6.842	7.430	7.139	8.723	8.310	7.599	6.714	8.581	8.641	7.957	7.369	6.684
<i>DLWT_IQ</i>	7.123	6.688	7.298	6.962	8.533	8.119	7.438	6.569	8.398	8.448	7.814	7.206	6.512
<i>DWT_FFT</i>	6.278	5.821	6.393	6.084	7.685	7.249	6.566	5.694	7.526	7.588	6.926	6.311	5.656
<i>DLWT_FFT</i>	6.106	5.624	6.191	5.883	7.477	6.947	6.363	5.493	7.320	7.377	6.717	6.124	5.500
<i>IQ+SPIHT</i>	7.312	6.867	7.435	7.135	8.737	8.320	7.606	6.689	8.595	8.649	7.987	7.370	6.671

TABLE VI  
NUMBER OF ACTUAL CODING COEFFICIENTS

Image	1.0 bpp				3.0 bpp				5.0 bpp			
	<i>DWT</i>	<i>DLWT</i>	<i>DWT</i>	<i>DLWT</i>	<i>DWT</i>	<i>DLWT</i>	<i>DWT</i>	<i>DLWT</i>	<i>DWT</i>	<i>DLWT</i>	<i>DWT</i>	<i>DLWT</i>
	<i>_IQ</i>	<i>_IQ</i>	<i>_FFT</i>	<i>_FFT</i>	<i>_IQ</i>	<i>_IQ</i>	<i>_FFT</i>	<i>_FFT</i>	<i>_IQ</i>	<i>_IQ</i>	<i>_FFT</i>	<i>_FFT</i>
<i>Img1</i>	246379	377959	276372	361359	1056143	1302703	1133865	1293111	1707490	1807954	1798878	1831103
<i>Img9</i>	290802	366788	305415	357026	1035667	1177413	1086394	1178763	1724939	1817767	1780948	1814229
<i>Img13</i>	239710	348618	256931	331036	1140841	1290093	1238720	1284356	1846514	1922798	1952499	1970038

up to 1.66 dB gain in PSNR and 0.282 MPE reduction. Compared with IQ-based coding schemes, the FFT program shows up to 0.48 dB gain in PSNR and 0.295 reduction in MPE. Moreover, compared with the SPIHT, DLWT\_IQ shows up to 2.00 dB gain in PSNR and 0.091 reduction in MPE, and DLWT\_FFT shows up to 2.24 dB gain in PSNR and 0.090 reduction in MPE.

*B. Contribution of DLWT and FFT Program*

Compared with the DWT-based coding schemes, the DLWT-based coding schemes requires lower bit rate for the same distortion. For the tested 13 complex SAR images, as shown in Table V, the required coding rates are 7.47 bpp for DLWT\_IQ, 7.64 bpp for DWT\_IQ, 6.39 bpp for DLWT\_FFT, and 6.60 bpp for DWT\_FFT. It is seen that the DLWT saves 2.2% and 3.1%

coding bits for IQ and FFT algorithms, respectively. Shown in Table VI, DLWT achieves higher coding efficiency because the coded coefficient numbers of DLWT are 53.41% in IQ and 30.75% in FFT larger than those of DWT, respectively. This is because of the better clustering capability of the DLWT than DWT, which requires fewer coding bits. Compared with the SPIHT, our algorithm also gains better performance.

Tables VII and VIII show the mean values of the 13 images. Again DLWT\_FFT and DLWT\_IQ outperform other schemes. From 0.5 bpp to 8.0 bpp, amplitude PSNR and MPE of DLWT-based coding scheme are always better than DWT counterparts. The PSNR of the FFT-based coding schemes is better than that of the IQ-based counterparts from 0.5 bpp to 6.0 bpp, but the MPE of the FFT-based coding schemes is better from 3.0 bpp to 5.5 bpp. For all the 13 images, the coding performance is similar with the average coding performance.

TABLE VII  
AVERAGE QUALITY GAIN BY DLWT IN PSNR (dB) AND MPE (RADIAN)

Bit Rate / bpp	0.5	1.0	1.5	2.0	2.5	3.0	3.5	4.0	4.5	5.0	5.5	6.0	6.5	7.0	7.5	8.0	
IQ	$\Delta PSNR$	1.324	1.276	0.944	0.927	1.097	1.107	0.921	0.921	0.708	0.492	0.710	0.421	0.659	0.716	0.867	0.913
	$\Delta MPE$	0.012	0.046	0.065	0.101	0.127	0.117	0.103	0.100	0.101	0.103	0.091	0.066	0.063	0.040	0.045	0.025
FFT	$\Delta PSNR$	0.855	1.191	1.039	1.345	1.431	1.471	1.370	1.376	1.120	0.977	1.057	0.704	0.819	0.845	0.877	0.938
	$\Delta MPE$	0.0078	0.165	0.139	0.127	0.154	0.162	0.116	0.132	0.115	0.102	0.108	0.076	0.074	0.048	0.045	0.026

TABLE VIII  
AVERAGE QUALITY GAIN BY FFT IN PSNR (dB) AND MPE (RADIAN)

Bit Rate / bpp	0.5	1.0	1.5	2.0	2.5	3.0	3.5	4.0	4.5	5.0	5.5	6.0	6.5	7.0	7.5	8.0
$\Delta PSNR$	0.115	0.124	0.181	0.158	0.198	0.182	0.231	0.237	0.282	0.284	0.321	0.086	-0.954	-2.480	-3.636	-4.646
$\Delta MPE$	-0.090	-0.048	-0.026	-0.010	-0.001	0.002	0.005	0.004	0.005	0.003	0.002	-0.004	-0.015	-0.026	-0.032	-0.036

TABLE IX  
COMPARISONS OF CODING PERFORMANCE FOR PSNR (dB)

Image	0.5 bpp				1.0 bpp				1.5 bpp			
	<i>SPIHT</i> (3 level)	<i>SPIHT</i> (7 level)	<i>CCSDS</i>	<i>DLWT</i> + <i>BPE</i>	<i>SPIHT</i> (3 level)	<i>SPIHT</i> (7 level)	<i>CCSDS</i>	<i>DLWT</i> + <i>BPE</i>	<i>SPIHT</i> (3 level)	<i>SPIHT</i> (7 level)	<i>CCSDS</i>	<i>DLWT</i> + <i>BPE</i>
<i>Img1</i>	68.50	71.88	71.86	71.98	71.53	74.47	74.61	74.69	74.20	76.87	76.84	76.94
<i>Img3</i>	65.19	72.05	71.71	71.80	70.92	74.42	74.58	74.68	73.66	76.53	76.64	76.77
<i>Img5</i>	60.29	63.68	63.75	63.84	63.58	66.03	66.16	66.27	65.90	68.43	68.56	68.88
<i>Img6</i>	55.73	64.30	64.32	64.38	62.45	66.82	67.10	67.17	65.58	69.23	69.31	69.38
<i>Img8</i>	61.42	70.15	70.16	70.26	68.61	72.61	72.81	72.92	71.31	75.06	75.09	75.18

TABLE X  
COMPARISONS OF CODING PERFORMANCE FOR SSIM

Image	0.5 bpp				1.0 bpp				1.5 bpp			
	<i>SPIHT</i> (3 level)	<i>SPIHT</i> (7 level)	<i>CCSDS</i>	<i>DLWT</i> + <i>BPE</i>	<i>SPIHT</i> (3 level)	<i>SPIHT</i> (7 level)	<i>CCSDS</i>	<i>DLWT</i> + <i>BPE</i>	<i>SPIHT</i> (3 level)	<i>SPIHT</i> (7 level)	<i>CCSDS</i>	<i>DLWT</i> + <i>BPE</i>
<i>Img1</i>	0.1621	0.5510	0.5938	0.6099	0.5542	0.7363	0.7588	0.7668	0.7283	0.8277	0.8541	0.8577
<i>Img3</i>	0.0926	0.4600	0.5380	0.5603	0.4251	0.6807	0.7111	0.7272	0.6584	0.8077	0.8296	0.8376
<i>Img5</i>	0.0907	0.4410	0.4784	0.5084	0.4559	0.6509	0.6970	0.7130	0.6603	0.7827	0.8117	0.8220
<i>Img6</i>	0.0277	0.3927	0.4418	0.4723	0.3096	0.6358	0.6729	0.6881	0.5681	0.7584	0.7935	0.8020
<i>Img8</i>	0.0345	0.5144	0.5457	0.5703	0.3889	0.7079	0.7387	0.7514	0.6419	0.8105	0.8416	0.8482

### C. Coding Performance of Amplitude SAR Images

The proposed DLWT-based coding schemes show performance gains over the DWT counterparts not only for complex SAR images but also for amplitude SAR images. DLWT+BPE also achieves coding performance gain in SPIHT. In the experiment, the decomposition levels of DWT and DLWT for SPIHT are three and seven, and the decomposition levels of DWT in CCSDS and DLWT in DLWT+BPE are three. Amplitude images of the complex SAR images in Fig. 9 are used. To compare the compression performance, we employ PSNR and SSIM [17], [18] as image quality assessments. The results of five amplitude SAR images at 0.5, 1.0, and 1.5 bpp are shown in Tables IX and X. Compared with the DWT-based coding algorithm, the

DLWT-based counterparts not only exhibit up to 0.13-dB gain in PSNR and 0.0305 gain in SSIM, but also show better visual quality. As Fig. 13 shows, DLWT+BPE shows the best visual quality in the edges and textures of complex SAR images.

## V. CONCLUSION

There are two main contributions in this paper. First, we propose two compression schemes, DLWT\_IQ and DLWT\_FFT, for the complex SAR images based on DLWT. The proposed two compression schemes significantly outperform DWT-based schemes in terms of higher PSNR and lower MPE. It is noteworthy that DLWT\_FFT outperforms DLWT\_IQ at low and middle bit rates, and thus can be applied for website browsing.

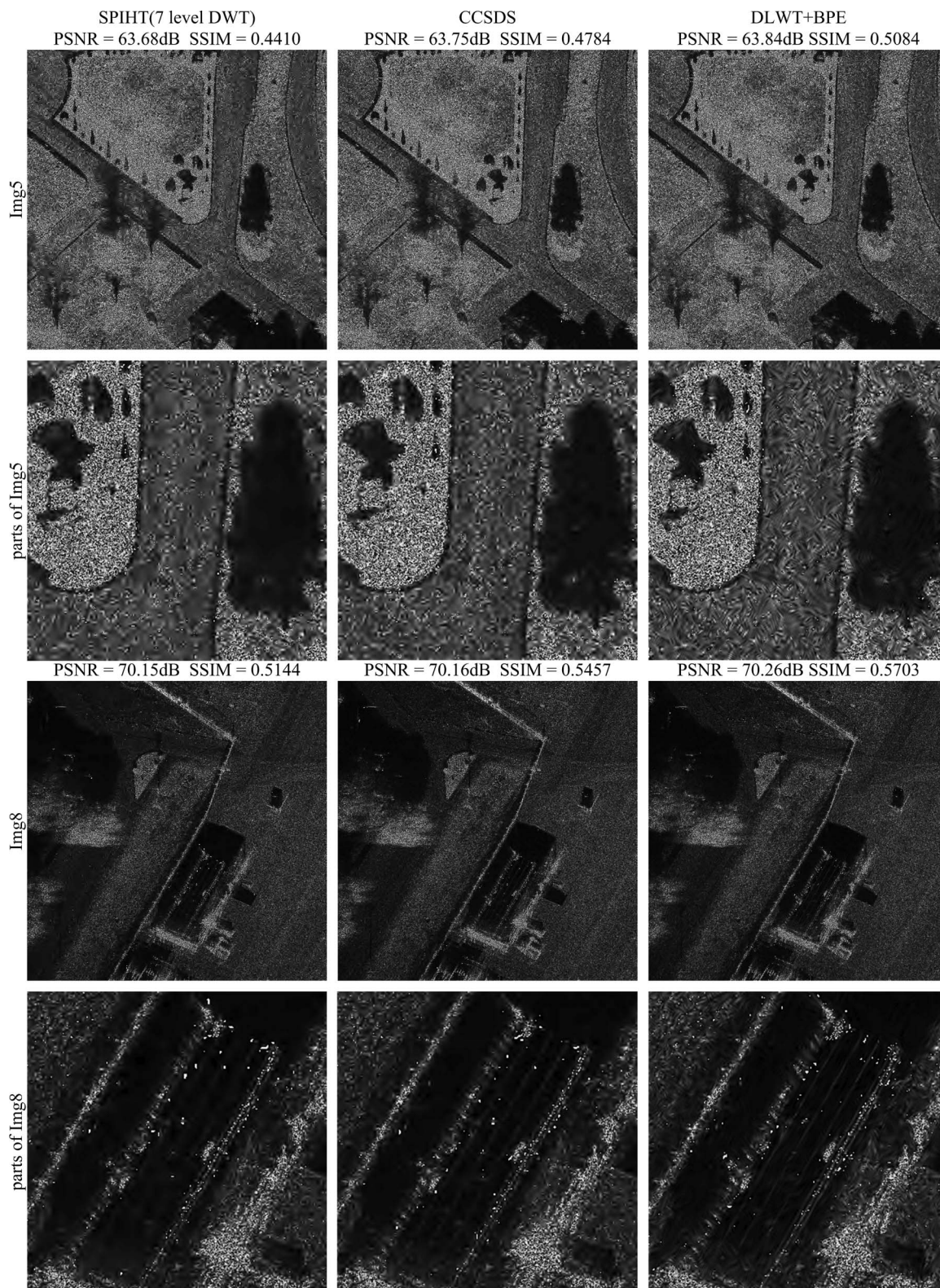


Fig. 13. Visual comparison of SPIHT, CCSDS, and DLWT+BPE at 0.5 bpp for Img5 and Img8.

Furthermore, both schemes preserve phases better than  $1^\circ$  and amplitudes better than 100 dB in PSNR, which is promising for a wide range of applications. Second, we observe a novel phenomenon, that is, for complex SAR images, DLWT provides higher clustering capability and the clustering capability can be captured by the BPE coding algorithm to improve the

rate-distortion performance when compared with DWT, even if the K-term approximation of DLWT is not as good as that of DWT. Hence, we may need other measures to assess the performance of representation for coding algorithm in addition to the classical K-term approximation. This is an interesting topic needing further investigation.

## ACKNOWLEDGMENT

The authors would like to thank the anonymous reviewers and editors for their careful review of this paper and many helpful suggestions that significantly improved the quality of this paper.

## REFERENCES

- [1] P. Eichel and R. W. Ives, "Compression of complex-valued SAR images," *IEEE Trans. Image Process.*, vol. 8, no. 10, pp. 1483–1487, Oct. 1999.
- [2] M. Sun and C. Li, "An adaptively weighted method based approach for data compression of complex-valued SAR images in frequency domain," in *Proc. IEEE Int. Geosci. Remote Sens. Symp.*, Jul. 2005, vol. 7, pp. 4704–4707.
- [3] S. Mallat, *A Wavelet Tour of Signal Processing: The Sparse Way*, 3rd ed. Orlando, FL: Academic, 2008.
- [4] A. M. Atto, D. Pastor, and A. Isar, "On the statistical decorrelation of the wavelet packet coefficients of a band-limited wide-sense stationary random process," *Signal Process.*, vol. 87, no. 10, pp. 2320–2335, Oct. 2007.
- [5] S. A. Werness, S. C. Wei, and R. Carpinella, "Experiments with wavelets for compression of SAR data," *IEEE Trans. Geosci. Remote Sens.*, vol. 32, no. 1, pp. 197–201, Jan. 1994.
- [6] M. Brandfass, W. Coester, and U. Benz, "Wavelet based approaches for efficient compression of complex SAR image data," in *Proc. IEEE Int. Geosci. Remote Sens. Symp.*, Aug. 1997, vol. 4, pp. 2024–2027.
- [7] R. W. Ives, C. Kiser, and N. Magotra, "Wavelet compression of complex SAR imagery using complex-and real-valued wavelets: A comparative study," in *Proc. IEEE Asilomar Conf. Signals, Syst. Comput.*, Nov. 1998, vol. 2, pp. 1294–1298.
- [8] J. M. Heermans, R. Rouse, and C. Chang, "Wavelet/trellis coded quantization of complex SAR imagery," in *Proc. IEEE 29th Appl. Imagery Pattern Recognit. Workshop*, Oct. 2000, pp. 121–128.
- [9] R. Dong, B. Hou, and S. Wang, "SAR image compression based on wedgelet-wavelet," *Signal Process. Image Enhancement Multimedia Process.*, vol. 31, pp. 67–75, Dec. 2007.
- [10] B. Li, R. Rui, and H. X. Jiang, "Remote-sensing image compression using two-dimensional oriented wavelet transform," *IEEE Trans. Geosci. Remote Sens.*, vol. 49, no. 1, pp. 236–250, Jan. 2011.
- [11] M. N. Do and M. Vetterli, "The contourlet transform: An efficient directional multiresolution image representation," *IEEE Trans. Image Process.*, vol. 14, no. 12, pp. 2091–2106, Dec. 2005.
- [12] W. Ding, F. Wu, and X. Wu, "Adaptive directional lifting-based wavelet transform for image coding," *IEEE Trans. Image Process.*, vol. 16, no. 2, pp. 416–427, Feb. 2007.
- [13] Y. Liu and K. N. Ngan, "Weighted adaptive lifting-based wavelet transform for image coding," *IEEE Trans. Image Process.*, vol. 17, no. 4, pp. 500–511, Apr. 2008.
- [14] X. S. Hou, G. F. Jiang, R. Ji, and C. L. Shi, "Directional lifting wavelet and universal trellis coded quantization based image coding algorithm and objective quality evaluation," *IET Image Process.*, vol. 5, no. 8, pp. 693–702, Dec. 2011.
- [15] F. Garcia-Vilchez and J. Serra-Sagrasta, "Extending the CCSDS recommendation for image data compression for remote sensing scenarios," *IEEE Trans. Geosci. Remote Sens.*, vol. 47, no. 10, pp. 3431–3445, Oct. 2009.
- [16] Consultative Committee for Space Data Systems, *Image Data Compression CCSDS 120.1-G-1*, Washington, DC: CCSDS, Jun. 2007. [Online]. Available: <http://public.ccsds.org/publications/archive/120x1g1e2.pdf>
- [17] Z. Wang, A. Bovik, H. Sheikh, and E. Simoncelli, "Image quality assessment: From error visibility structural similarity," *IEEE Trans. Image Process.*, vol. 13, no. 4, pp. 600–612, Apr. 2004.
- [18] Z. Wang, *The SSIM Index for Image Quality Assessment*, last retrieved in May 13, 2009. [Online]. Available: <http://www.ece.uwaterloo.ca/~z70wang/research/ssim>
- [19] G. J. Sullivan and R. L. Baker, "Efficient quadtree coding of images and video," *IEEE Trans. Image Process.*, vol. 3, no. 3, pp. 327–331, May 1994.
- [20] Advanced Video Coding, ITU-T Rec. H.264 and ISO/IEC 14496-10, 2003.
- [21] Sandia National Laboratories, *Sandia SAR Data*. [Online]. Available: <http://www.sandia.gov/radar/sar-data.html>
- [22] S. Amir and A. P. Pearlman, "A new fast and efficient image codec based on set partitioning in hierarchical trees," *IEEE Trans. Circuits Syst. Video Technol.*, vol. 6, no. 3, pp. 243–250, Jun. 1996.
- [23] S. Mustafa and A. P. William, *Set Partitioning in Hierarchical Trees (SPIHT) Algorithm*. [Online]. Available: <http://www.cipr.rpi.edu/research/SPIHT>



**Xingsong Hou** received the Ph.D. degree from Xi'an Jiaotong University, Xi'an, China, in 2005.

Now, he is an Associate Professor with the School of Electronics and Information Engineering, Xi'an Jiaotong University. His research interests include video/image coding, wavelet analysis, sparse representation, sparse representation and compressive sensing, and radar signal processing. During October 2010–2011, he was a Visiting Scholar at Columbia University, New York.



**Jing Yang** received the B.S. and M.S. degrees from Xi'an Jiaotong University, Xi'an, China, in 2008 and 2011, respectively.

Her research interests include video/image coding, sparse representation, and compressive sensing.



**Guifeng Jiang** received the B.S. degree from Xi'an Technological University, Xi'an, China, in 2007, and the M.S. degree from Xi'an Jiaotong University, Xi'an, in 2010.

Her research interests include video/image coding and wavelet analysis.



**Xueming Qian** (M'10) received the B.S. and M.S. degrees from the Xi'an University of Technology, Xi'an, China, in 1999 and 2004, respectively, and the Ph.D. degree from Xi'an Jiaotong University, Xi'an, China, in 2008.

He was awarded a Microsoft fellowship in 2006. From 1999 to 2001, he was an Assistant Engineer at Shannxi Daily. From 2008 until now, he has been a Faculty Member with the School of Electronics and Information Engineering, Xi'an Jiaotong University. He was a Visiting Scholar at Microsoft Research Asia from August 2010 to March 2011. His research interests include video/image analysis, indexing, and retrieval.

search Asia from August 2010 to March 2011. His research interests include video/image analysis, indexing, and retrieval.